J. Fluid Mech. (2003), *vol.* 491, *pp.* 259–274. © 2003 Cambridge University Press
DOI: 10.1017/S0022112003005421 Printed in the United Kingdom

Oscillatory thermocapillary convection in open cylindrical annuli. Part 2. Simulations

By BOK-CHEOL SIM[1]†, ABDELFATTAH ZEBIB[1] AND DIETRICH SCHWABE[2]

[1]Department of Mechanical and Aerospace Engineering, Rutgers, The State University of New Jersey, Piscataway, NJ 08855-8058, USA

[2]I. Physikalisches Institut, Justus-Liebig-Universität, Heinrich-Buff-Ring 16, 35392 Giessen, Germany

(Received 6 July 2001 and in revised form 15 January 2003)

Oscillatory thermocapillary convection in open cylindrical annuli heated from the outer wall is investigated numerically. Results at fixed inner/outer radius ratio of 0.5, aspect ratios (*Ar*) of 1, 2.5, 3.33, and 8, zero Biot number, and a Prandtl number of 6.84 are obtained and compared with experiments (Part 1 of this paper). Convection is steady and axisymmetric at sufficiently low values of the Reynolds number (*Re*). Transition to oscillatory states occurs at critical values of *Re* which depend on *Ar*. With $Ar = 1$, 2.5 and 3.33, we observe 5, 9 and 12 azimuthal wavetrains, respectively, travelling clockwise at the free surface near the critical *Re*. With $Ar = 8$, there are 20 standing waves near the critical *Re*. Experimental results in Part 1 support this finding. A multi-roll structure appears beyond the critical *Re* in shallow liquid layers with $Ar = 3.33$ and 8. The critical *Re* and frequency are in qualitative but not in quantitative agreement with the experimental ones. Either heat loss from the free surface or heating from the surroundings to the free surface stabilizes the flow, and the critical *Re* increases with increasing Biot number while the critical period goes down. The numerical results agree better with the experimental ones if the free surface is assumed to be heated as shown in Part 1. We have also computed supercritical time-dependent states and find that while the non-dimensional frequency increases with increasing *Re* near the critical region, it approaches an asymptote at supercritical *Re*.

1. Introduction

Since Chang & Wilcox (1976) found that thermocapillarity plays an important role in crystal growth a number of investigations have treated thermocapillary convection. Smith & Davis (1983) discussed the instability mechanisms using linear stability theory of flows in an infinite liquid layer. Kuhlmann & Rath (1993) considered the linear instability of steady axisymmetric thermocapillary flow in a cylindrical liquid bridge with an aspect ratio of 1. They found that the most dangerous disturbance was either a pure hydrodynamic steady mode or an oscillatory hydrothermal wave, depending on *Pr*. Wanschura *et al.* (1995) further investigated the primary instability of axisymmetric steady thermocapillary flow in a cylindrical liquid bridge, and

---

† Present address: Department of Mechanical Engineering, Hanyang University, Ansan, Kyunggi-Do 425-791, Korea.

confirmed the earlier results of Neitze *et al.* (1993). Savino & Monti (1996) showed the oscillatory behaviour of temperature and velocity profiles in liquid bridges using three-dimensional simulations. Their studies revealed two-lobed rotating as well as pulsating isotherm patterns.

A rich body of thermocapillary problems in open rectangular cavities have been numerically investigated. Peltier & Biringen (1993) provided a stability diagram as a function of aspect ratio with a $Pr = 6.78$ liquid in two-dimensional rectangular cavities. They found a critical aspect ratio near 2.3 and minimum critical Marangoni number near 20 000. Sab, Kuhlmann & Rath (1996) investigated steady three-dimensional thermocapillary convection in an open cubic container. They showed the damping effect of the front and back walls on the temperature field by comparing three-dimensional with two-dimensional simulations in steady state flows. Xu & Zebib (1998) studied oscillatory thermocapillary-driven convection in an open cavity using two- and three-dimensional simulations. They found that there were two disjoint neutral curves for $Pr \leqslant 4.4$, and that the existence of spanwise waves could reduce the critical Re. Three-dimensional simulations of thermocapillary convection in an open cylindrical annulus were first reported by Sim & Zebib (2002*a*). Four kinds of isotherm patterns at the free surface were observed with increasing Re: a two- and a three-lobed clockwise rotating pattern, and a two- and a three-lobed pulsating pattern. They found that heat loss from the free surface provided an explanation for the dependence of the critical Marangoni number Ma_c on the container size at fixed aspect ratio which was observed in experiments (Kamotani, Ostrach & Masud 2000).

While two-dimensional models of open rectangular cavities predicted oscillatory thermocapillary convection (Xu & Zebib 1998), it could not be realized in axisymmetric simulations with open cylinders (Sim & Zebib 2002*b*). Thus, a three-dimensional model is necessary to compute these flows. In the present paper we report numerical results on oscillatory thermocapillary convection in open cylindrical containers heated from the outer wall, constituting a model for the Czochralski crystal growth system sketched in figure 1(*a*). The influence of the aspect ratio on the critical Reynolds numbers and frequencies, and the pattern of convection is studied and compared with available experimental results.

2. Mathematical model

The physical system is shown in figure 1 of Part 1 (Schwabe, Zebib & Sim 2003) for the microgravity experiment MAGIA, and the parameters are shown in figure 1(*b*). It is a cylindrical annulus with inner and outer radii, R_i and R_o, which is filled with an incompressible, Newtonian fluid of Prandtl number 6.84 to a height H. The aspect ratio, Ar, is defined as $(R_o - R_i)/H$, and the values of Ar are 1, 2.5, 3.33, and 8 (which correspond to different values of H with R_i and R_o fixed, $R_i/R_o = 0.5$). The vertical inner and outer walls have temperatures, $T_i = T_{cold}$ and $T_o = T_{hot}$, respectively. The bottom is an adiabatic solid wall. The horizontal free surface is assumed non-deformable and has convective heat loss to the surroundings with the ambient temperature, $T^*_\infty (= T_{cold})$. The surface tension is assumed a linear function of temperature,

$$\sigma = \sigma_r - \gamma(T^* - T^*_r) \tag{2.1}$$

where $\gamma = -\partial\sigma/\partial T^*$, and subscript r and superscript $*$ represent a reference state and dimensional quantity.

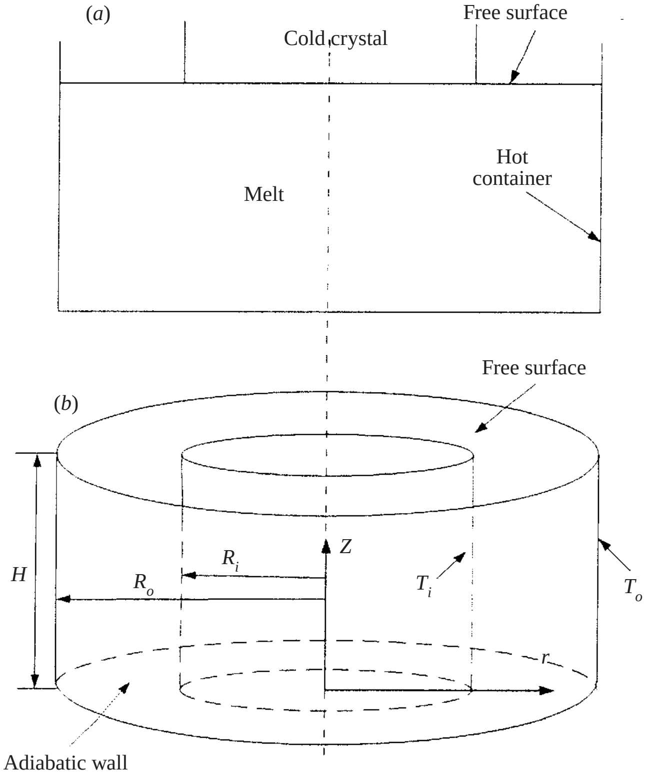

FIGURE 1. (*a*) The Czochralski technique and (*b*) the physical system. The aspect ratio $Ar = (R_o - R_i)/H$ of the annular gap can be changed between 8 and 1 by adjusting H with a movable bottom.

In a microgravity environment, the non-dimensional governing equations are as follows:

$$\nabla \cdot \boldsymbol{v} = 0, \tag{2.2}$$

$$Re\left(\frac{\partial \boldsymbol{v}}{\partial t} + \nabla \cdot (\boldsymbol{v}\boldsymbol{v})\right) = -\nabla P + \nabla^2 \boldsymbol{v}, \tag{2.3}$$

$$Ma\left(\frac{\partial T}{\partial t} + \nabla \cdot (\boldsymbol{v}T)\right) = \nabla^2 T, \tag{2.4}$$

where $\boldsymbol{v}$ is the non-dimensional velocity vector, and P and T are the non-dimensional pressure and temperature. Re is the Reynolds number, Pr is the Prandtl number, and Ma is the Marangoni number defined by

$$Re = \gamma \frac{\Delta T H}{\nu \mu}, \qquad Pr = \frac{\nu}{\alpha}, \qquad Ma = Pr\, Re, \tag{2.5}$$

where ν, μ, and α are kinematic viscosity, dynamic viscosity, and thermal diffusivity respectively. The length, velocity, pressure, and time are normalized with respect to H, $\gamma \Delta T/\mu$, $\gamma \Delta T/H$, and $\mu H/\gamma \Delta T$, respectively, where $\Delta T = T_{hot} - T_{cold}$. Non-dimensional temperature, T, is defined by $T = (T^* - T_{cold})/\Delta T$.

The velocities in the r-, θ-, and z-directions of a cylindrical coordinate system are u, v, and w, respectively. With the free surface assumed non-deformable, the boundary

	Grid numbers ($r \times z \times \theta$)	Critical Re	Azimuthal waves
(a)	$51 \times 51 \times 21$	740	5
	$61 \times 61 \times 31$	740	5
	$71 \times 71 \times 41$	740	5
(b)	$51 \times 41 \times 31$	510	
	$61 \times 51 \times 41$	490	9
	$71 \times 61 \times 51$	490	9
(c)	$61 \times 51 \times 41$	490	13
	$61 \times 51 \times 61$	490	12
	$71 \times 61 \times 51$	490	12
	$71 \times 61 \times 81$	490	12
(d)	$61 \times 41 \times 51$	600	24
	$71 \times 51 \times 56$	570	24
	$71 \times 51 \times 80$	570	21
	$71 \times 51 \times 100$	560	20
	$71 \times 51 \times 112$	560	20

TABLE 1 Grid refinement studies with $Bi = 0$ and (a) $Ar = 1$, (b) $Ar = 2.5$, (c) $Ar = 3.3$, and (d) $Ar = 8$.

conditions become

$$\frac{\partial u}{\partial z} + \frac{\partial T}{\partial r} = 0, \quad \frac{\partial v}{\partial z} + \frac{1}{r}\frac{\partial T}{\partial \theta} = 0, \quad w = 0, \quad \frac{\partial T}{\partial z} = -Bi\,T \quad \text{at} \quad z = 1, \tag{2.6}$$

$$u = 0, \quad v = 0, \quad w = 0, \quad \frac{\partial T}{\partial z} = 0 \quad \text{at} \quad z = 0, \tag{2.7}$$

$$u = 0, \quad v = 0, \quad w = 0, \quad T = 0 \quad \text{at} \quad r = R_i/H, \tag{2.8}$$

$$u = 0, \quad v = 0, \quad w = 0, \quad T = 1 \quad \text{at} \quad r = R_o/H. \tag{2.9}$$

The Biot number in equation (2.6) is given by $Bi = hH/k$ where h is a heat transfer coefficient to the surroundings at the cold wall temperature, and k is the thermal conductivity of the liquid.

3. Numerical aspects

The governing equations (2.2)–(2.4) and (2.6)–(2.9) are solved by a finite volume scheme with second-order accuracy in space and with an implicit method in time. The SIMPLER algorithm of Patankar (1980) is used to handle the pressure coupling. Non-uniform grids (grid-stretching factor 1.1) are constructed with finer meshes in the regions under the free surface and near the bottom and sidewalls where boundary layers develop. The azimuthal direction has uniform grids in all cases. All computations are started with either zero or steady-state initial conditions at lower Re. In order to examine grid dependence, critical Reynolds numbers, Re_c, which are the largest Re resulting in steady states, are computed with various grids in each aspect ratio. Convergence criteria for a steady state are $|s^{n+1} - s^n| \leqslant 10^{-10}$ and $|s^{n+1} - s^n|/|s^{n+1}| \leqslant 10^{-4}$, where s is any of the variables (u, v, w, T) at all points and n is the time marching level. In addition, time histories of velocities and temperatures at the mid-point of the free surface, computed with various grids and time steps, are compared. Table 1 shows Re_c found using different grids with $Ar = 1$, 2.5, 3.33 and 8, respectively. Re is varied in increments of 10 in order to estimate Re_c. These steps

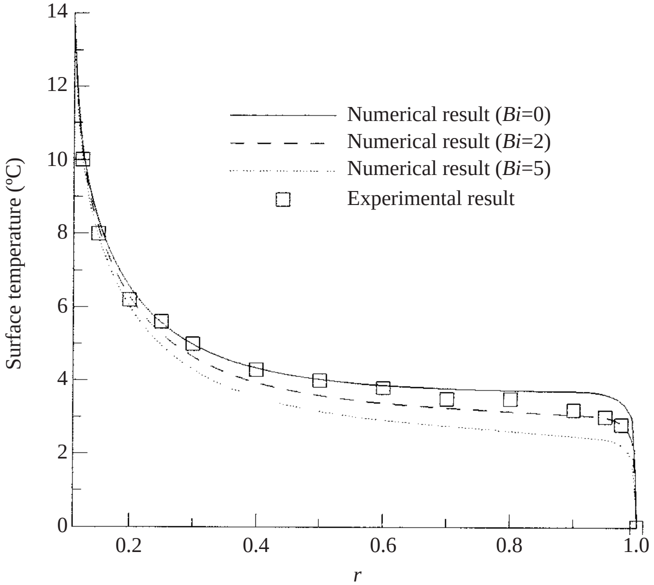

FIGURE 2. Surface temperature distribution $(T^* - T_o)$ with $Pr = 97$, $Re = 510$, $Ar = 0.889$ $(R_i/H = 0.111,\ R_o/H = 1)$, $T_i = T_{hot}$ and $T_o = T_{cold}$. The numerical results with $Bi = 2$ are in good agreement with experiments (Kamotani *et al.* 1995).

$(\Delta Re = 10)$ are less than 3% of the reported Re_c. The errors in the reported values of Re_c can be as large as 8% with $Ar = 8$.

The numerical code is also validated by comparison of steady surface temperature distribution with experimental results (Kamotani, Ostrach & Pline 1995) with reversed heating (hot inner and cold outer walls), $T_i = 44\,^\circ\mathrm{C}$ and $T_o = 30\,^\circ\mathrm{C}$, and $R_o = 5\,\mathrm{cm}$, $R_i = 0.555\,\mathrm{cm}$ and $H = 5\,\mathrm{cm}$ with 10 cSt silicone oil. The parameters for the simulation are $Pr = 97$, $Ar = 0.889$ and $Re = 510$. The numerical results with $Bi = 2$ are in good agreement with those from experiments as shown in figure 2.

4. Results and discussion

4.1. *Azimuthal flow structures with* $Bi = 0$

Re_c for onset of oscillations with $Ar = 1$ is 740. At $Re = 740$, the flow is steady and the isotherms on the free surface are circular lines, i.e. axisymmetric. Figure 3 shows the time history of the temperature near the mid-point $(r = 1.45,\ z = 1,\ \theta = 0)$ of the free surface with various supercritical Re. Figure 3(*a*) is computed from zero initial conditions, and figures 3(*b*) and 3(*c*) are computed from the same steady-state initial conditions $(Re = 700)$. As expected, starting from the same initial conditions oscillations begin earlier in time at the higher Re. While the amplitudes of temperature oscillations are larger at the higher Re, the mean temperature at these points decreases with increasing Re. All calculations were continued until a time-asymptotic state was reached as shown in figure 3.

Figure 4 shows instantaneous temperature distributions on the free surface with various Re, with figures 4(*a*) and 4(*b*) corresponding to the last time of figures 3(*a*) and 3(*c*), respectively. The pattern of five azimuthal waves remains unchanged with increasing Re. Figures 5(*a*) and 5(*b*) show one cycle of the free surface isotherm $(T = 0.8)$, and of the temperature oscillations at a fixed radial location on the

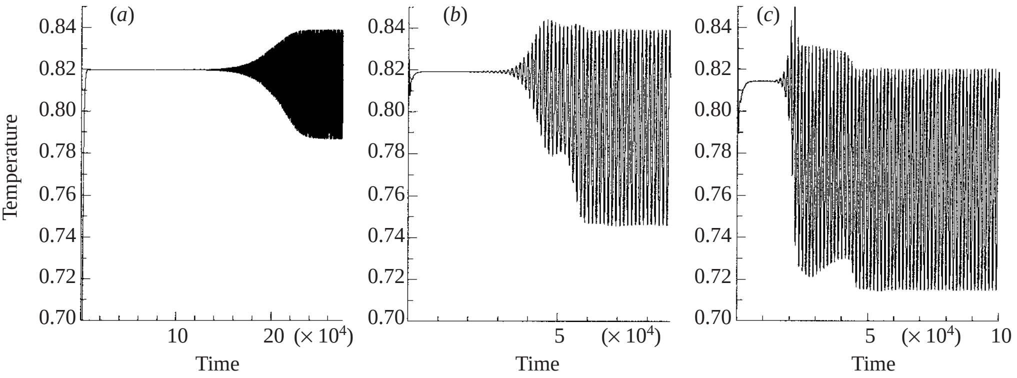

FIGURE 3. Time history of the temperature near the mid-point of the free surface with $Ar=1$, $Bi=0$ and (*a*) $Re=800$, (*b*) $Re=1000$ and (*c*) $Re=1500$. The same initial conditions are employed in (*b*) and (*c*). The oscillations begin earlier in time at the higher *Re*.

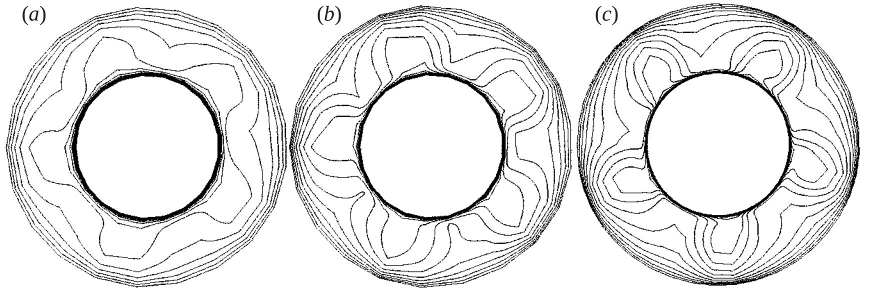

FIGURE 4. Surface temperature distribution with $Ar=1$, $Bi=0$ and (*a*) $Re=800$ (grid: $51(r)\times 51(z)\times 21(\theta)$), (*b*) $Re=1500$ ($51\times 51\times 21$) and (*c*) $Re=2500$ ($71\times 71\times 41$). The pattern of five waves remains unchanged with increasing *Re*.

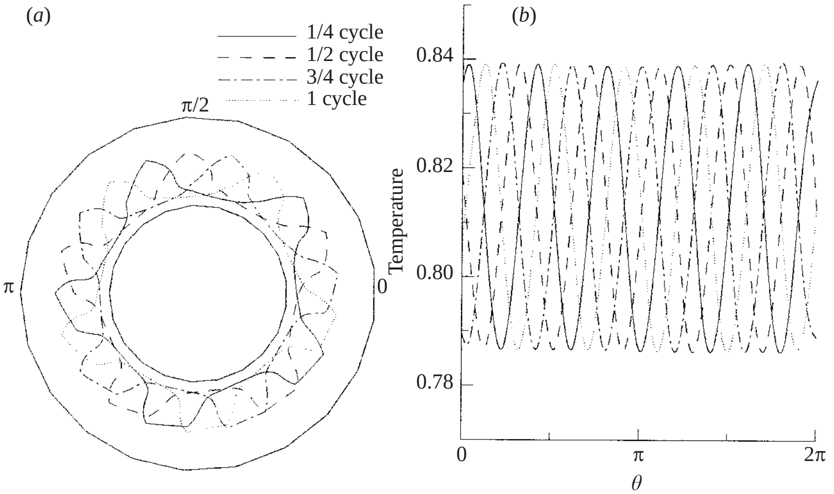

FIGURE 5. One cycle of (*a*) the free-surface isotherm ($T=0.8$) and (*b*) temperature oscillations at the free surface and $r=1.47$ with $Re=800$, $Ar=1$ and $Bi=0$. Five azimuthal waves are travelling clockwise.

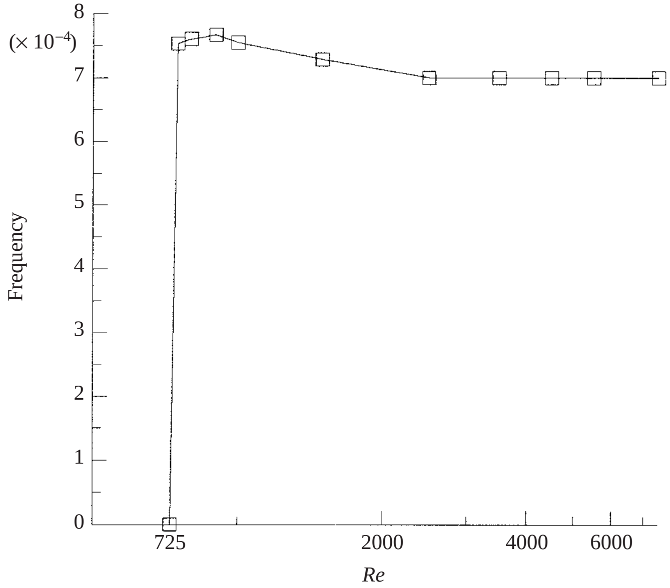

FIGURE 6. Frequency of temperature oscillations with various *Re*, for $Ar = 1$ and $Bi = 0$. While the frequency near Re_c increases with increasing *Re*, it approaches an asymptotic value in highly supercritical states.

free-surface with $Re = 800$. It is seen from figures 4 and 5 that five azimuthal waves are rotating clockwise in agreement with a similar finding in the experiments (figure 11*a* in Part 1). The isotherms have the same shape when rotated by $\frac{2}{5}\pi$. Thus if one measures the temperature at a fixed point on the free surface, the frequency of the temperature oscillations will be five times the isotherm rotation frequency.

Figure 6 shows the frequency (F), calculated by a Fourier decomposition of the temperature signal at a fixed point, corresponding to various *Re*. While F increases with increasing *Re* near the critical region, it decreases with increasing *Re* in the supercritical region until $Re = 2500$. Above $Re = 2500$, F is constant within the error bounds of the simulations. The F dependence on *Re* is in qualitative agreement with the two-dimensional results of Chen & Hwu (1993).

Re_c with $Ar = 2.5$ and 3.33 is found to be 490. The corresponding temperature distributions on the free surface are shown in figures 7 and 8. While nine azimuthal waves near the critical region appear on the free surface with $Ar = 2.5$, ten azimuthal waves are observed at $Re = 800$ as shown in figure 7. This is in reasonable agreement with the results from the experiments in figure 12(*c*) of Part 1, where 11 azimuthal waves are observed at $Re = 2.5Re_c(7500)$. With $Ar = 3.33$, the twelve azimuthal waves are rotating clockwise near the critical region in figure 8(*a*). It is evident that the number of azimuthal rotating waves near the critical region increases with increasing *Ar*.

Figures 9 and 10 show temperature fluctuations (deviation from the time-averaged mean temperature at each position) at the free surface and one cycle of temperature fluctuations at fixed radial locations on the free surface corresponding to figure 8(*b*). The source and sink at the free surface are observed near $\theta = \pi$ and 0, respectively. The waves travel both clockwise and counterclockwise from $\theta = \pi$ to $\theta = 0$. The fluctuations are stronger near the inner, cold wall as shown in figure 10.

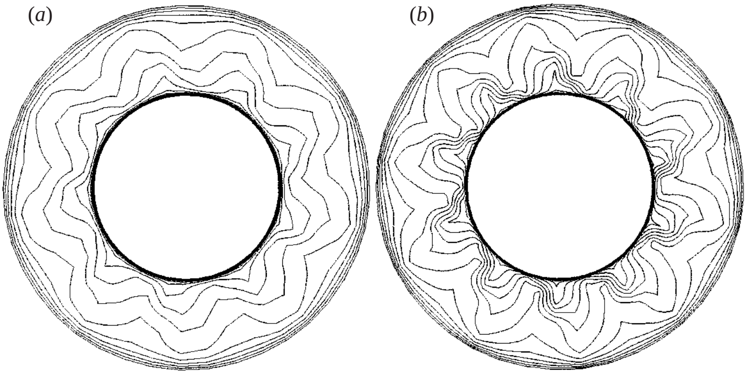

FIGURE 7. Temperature distribution on the free surface with $Ar = 2.5$, $Bi = 0$ and (*a*) $Re = 525$ and (*b*) $Re = 800$ (grid: $61 \times 51 \times 41$). The pattern of nine azimuthal waves in (*a*) changes as Re increases to ten waves in (*b*).

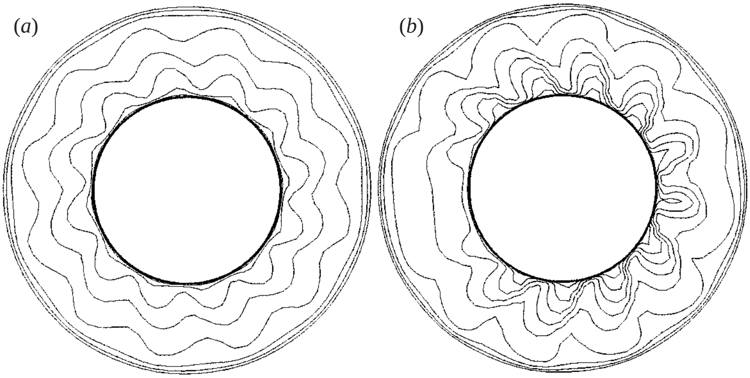

FIGURE 8. Temperature distribution on the free surface with $Ar = 3.33$, $Bi = 0$ and (*a*) $Re = 550$ and (*b*) $Re = 900$ (grid: $71 \times 61 \times 81$); (*a*) is a rotating wave and (*b*) is a wave pattern travelling from a source in the opposite direction to a sink.

A mesh of $71 \times 51 \times 112$ with $Ar = 8$ is necessary to resolve the increased number of azimuthal wavetrains. Re_c with $Ar = 8$ is 560. Figure 11 gives temperature distributions on the free surface with $Re = 625$, while temperature fluctuations on the free surface are shown in figures 12 and 13. Twenty azimuthal wavetrains are found on the free surface. The waves are pulsating, but not pure standing waves as shown in figure 13. The inner wall appears to be the source of the waves: the waves are generated at the inner cold wall and travel to the outer hot wall as shown in figure 14. This wave-propagation direction is in good agreement with the hydrothermal waves in the infinite-layer model (Smith & Davis 1983) and the rectangular cavity simulations (Xu & Zebib 1998). However, while the oscillations are stronger near the cold wall in the open annulus, they are stronger near the hot wall of the rectangular cavity (Xu & Zebib 1998). This difference may be due to a curvature effect. We thus have travelling r-waves and nearly standing θ-waves in cylindrical shallow liquid layers. As standing waves result from a linear superposition of a pair of counter-rotating waves, we can attribute the observed deviation from pure standing waves to strong nonlinearity and the superposed outward wave propagation. As Re increases these waves propagate far from the inner wall. The critical wavelength $\lambda = 2.5$ ($Pr = 6.84$) from linear theory

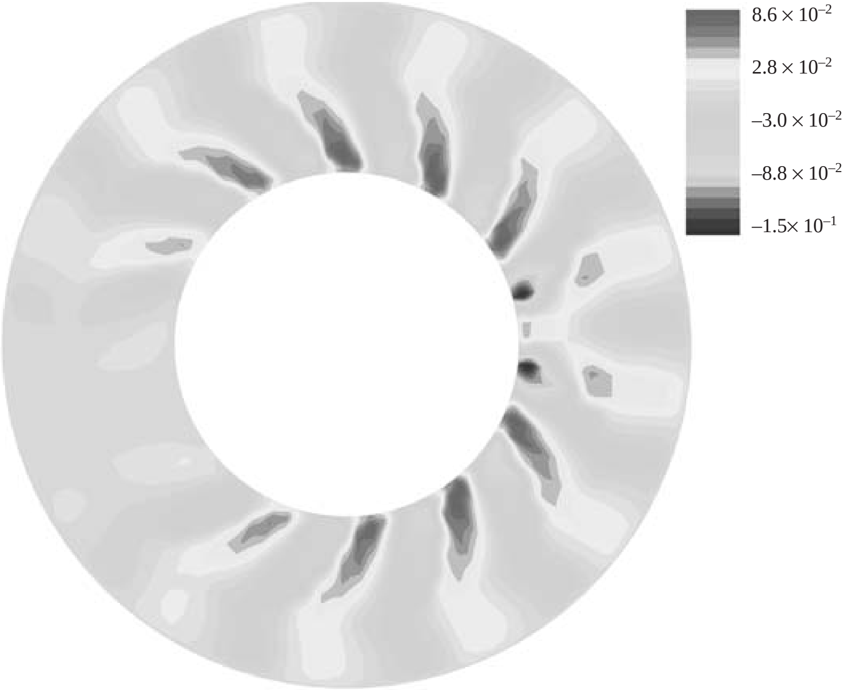

FIGURE 9. Snapshot of free-surface temperature fluctuations corresponding to figure 8(*b*) ($Ar = 3.33$, $Bi = 0$, $Re = 900$). A source and sink pattern is observed near $\theta = \pi$ and 0, respectively.

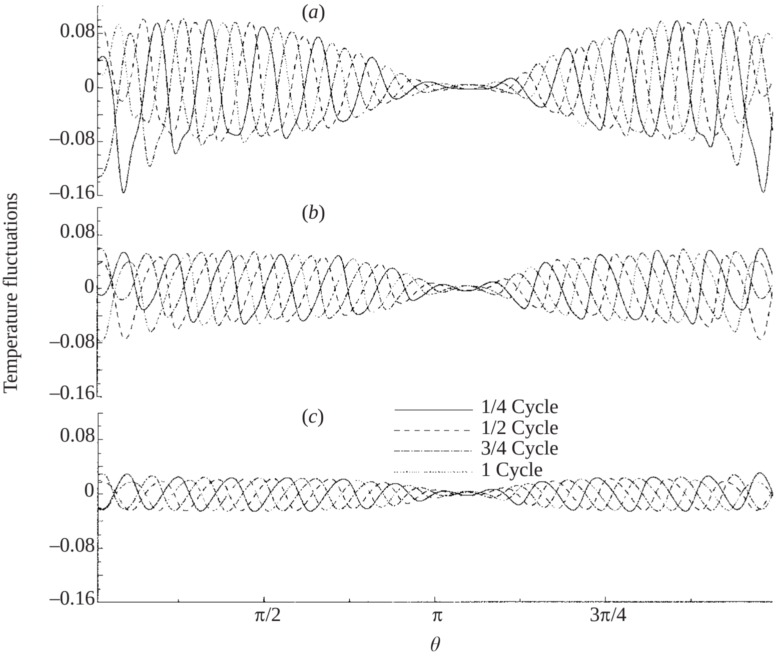

FIGURE 10. One cycle of temperature fluctuations at the free surface and (*a*) $r = 3.54$, (*b*) $r = 4.77$ and (*c*) $r = 6.37$ corresponding to figure 9 ($Ar = 3.33$, $Bi = 0$, $Re = 900$). The lines are from smooth interpolations through calculated points. The fluctuations decrease with increasing r towards the hot side.

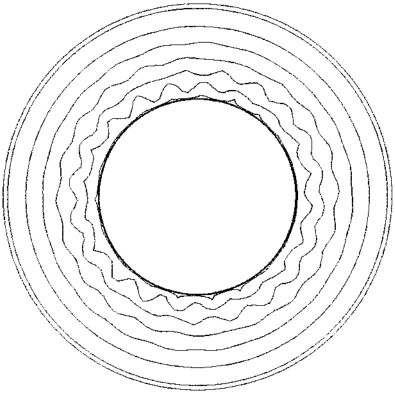

FIGURE 11. Temperature distributions on the free surface with $Ar = 8$, $Bi = 0$ and $Re = 625$ (grid: 71 × 51 × 112). The inner cold wall appears to be the source of the waves.

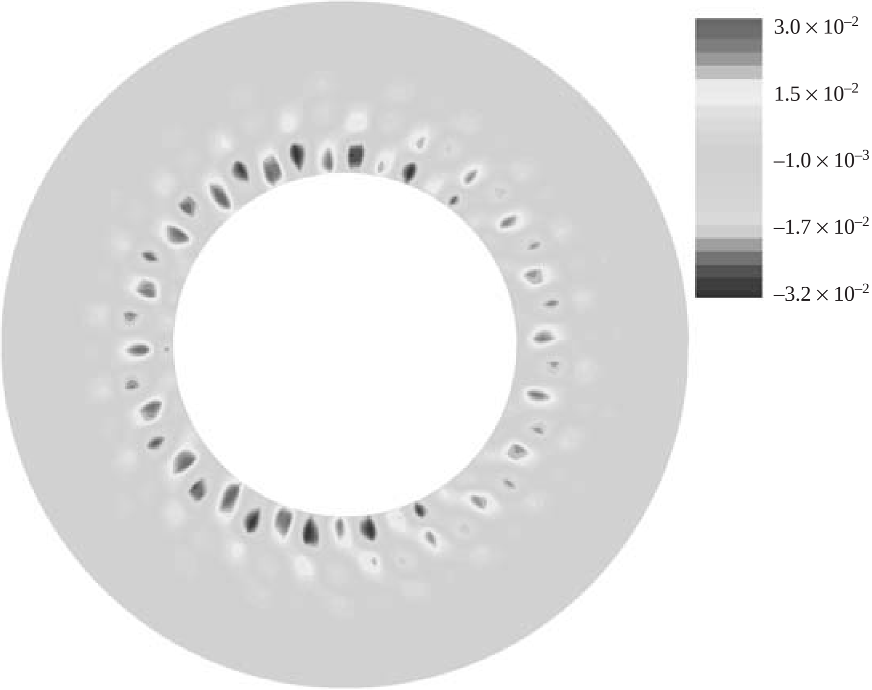

FIGURE 12. Snapshot of free-surface temperature fluctuations corresponding to figure 11 ($Ar = 8$, $Bi = 0$, $Re = 625$) indicating a standing wave pattern.

(Smith & Davis 1983) implies 20 waves at the inner wall, which is in good agreement with our numerical result. In addition, the angle of wave propagation between the temperature gradient and the wavevector varies from 50° to 60° at, respectively, $\theta = \pi/2$ and $3\pi/2$ as shown in figures 12 and 16(a). This is in good agreement with about 60° from linear theory and 40°–60° from experiments (Garnier & Chiffaudel 2001).

4.2. *Spiral and roll structures with* $Bi = 0$

Figure 15 shows shadowgraphic snapshots at the free surface with two values of Re and $Ar = 3.33$. Because the waves travel from the inner to the outer wall, and

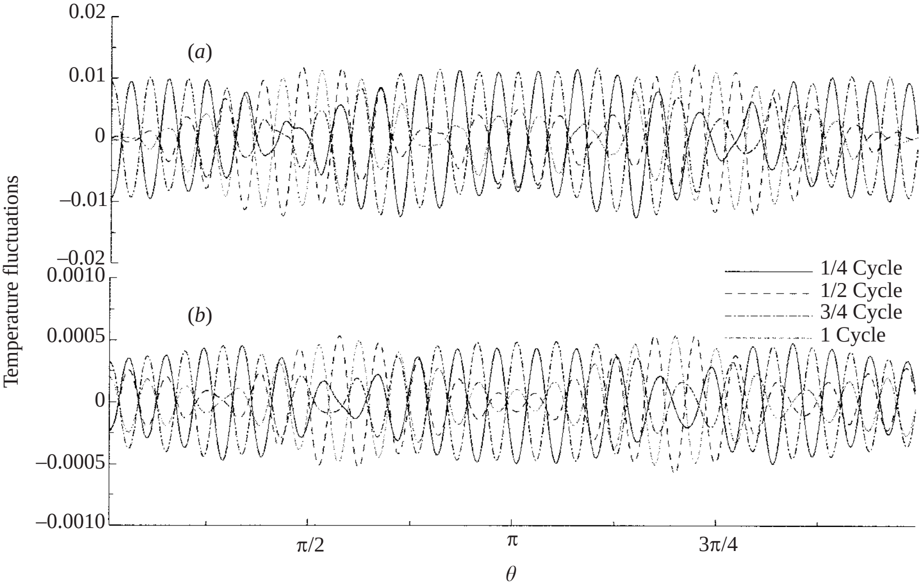

FIGURE 13. One cycle of the free-surface temperature fluctuations at (*a*) $r = 11.45$ and (*b*) $r = 15.3$ corresponding to figure 12 ($Ar = 8$, $Bi = 0$, $Re = 625$) confirming the standing wave nature of the phenomenon.

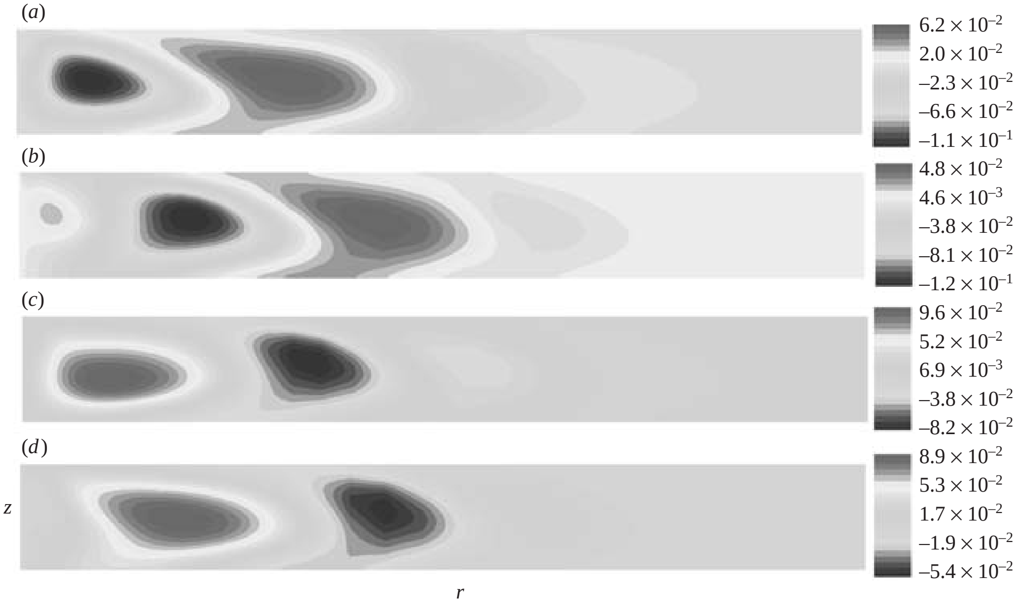

FIGURE 14. Snapshots of meridional temperature fluctuations ($\theta = 0$) at four evenly distributed instants within one cycle associated with figures 11, 12 and 13 ($Ar = 8$, $Bi = 0$, $Re = 625$). Waves travel from the inner cold to outer hot walls in qualitative agreement with the infinite-layer model (Smith & Davis 1983) and the rectangular cavity simulations (Xu & Zebib 1998).

rotate clockwise, a supercritical spiral structure appears on the free surface as shown in figure 15(*a*). At higher *Re*, a pattern with travelling r-waves and source–sink θ-waves which propagate from a source in opposite directions to a sink is shown in

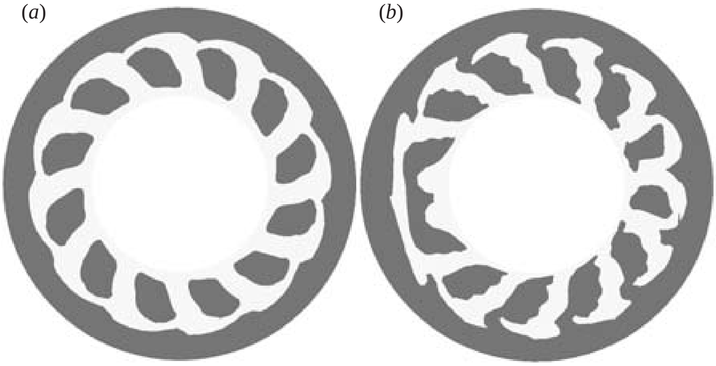

FIGURE 15. Shadowgraphic snapshots (contours of $\nabla^2 T$) at the free surface corresponding to figure 8 ($Ar = 3.33$, $Bi = 0$. (*a*) $Re = 550$ and (*b*) $Re = 900$): (*a*) shows azimuthal clockwise rotating waves, while (*b*) indicates azimuthal waves with a source and sink near respectively $\theta = \pi$ and 0.

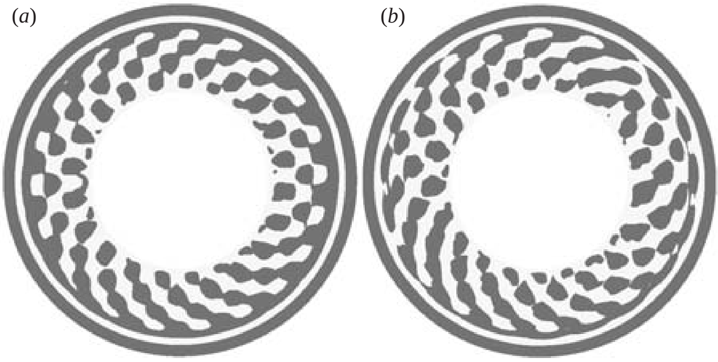

FIGURE 16. Shadowgraphic snapshots (contours of $\nabla^2 T$) at the free surface corresponding to figure 11 ($Ar = 8$, $Bi = 0$, (*a*) $Re = 625$ and (*b*) $Re = 700$). Both (*a*) and (*b*) show azimuthal standing waves with a source and sink near respectively $\theta = 0$ and π.

figure 15(*b*). However, with $Ar = 8$ figure 16 indicates that slightly supercritical convection is in the form of travelling r-waves and pulsating source–sink θ-waves. These two kinds of spiral patterns are in qualitative agreement with experimental results (Garnier & Chiffaudel 2001).

Figure 17 shows streamlines at Re_c with various Ar and $Bi = 0$. The flows are steady and axisymmetric. A single-roll structure is observed at each Ar. Figure 18 shows snapshots of meridional streamlines at $\theta = 0$ with various Ar and supercritical Re. At steady state, only the single-roll structure is available with $Ar = 1$, 2.5, 3.33 and 8. However, just above critical, two and three rolls are observed with $Ar = 3.33$ and 8, respectively. This agrees with figure 10 of Part 1 for $Ar = 8$. The number of rolls increases with increasing Ar. We can expect the multi-roll structure to appear beyond Re_c in the case of shallow liquid layers. The axisymmetric results are very different from those of two-dimensional rectangular cavities reported by Xu & Zebib (1998), where a critical Ar exists, the multi-structure appears at subcritical Re, and the flow can be stable with multi-structure in the restabilized region (highly supercritical Re). However, the structures of three-dimensional states in shallow cylindrical and

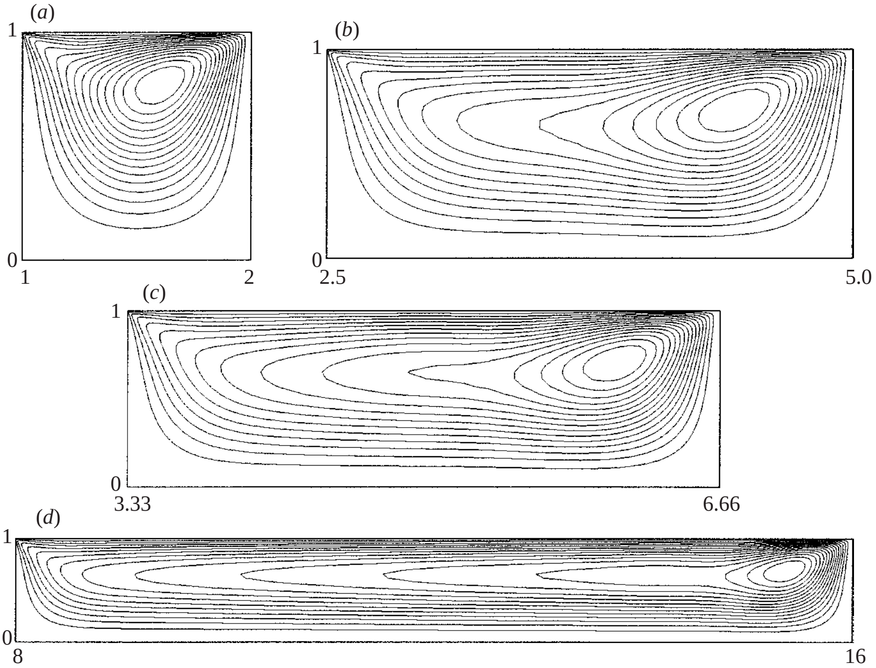

FIGURE 17. Streamlines at the critical steady state with $Bi = 0$, various Re_c and Ar: (*a*) 740 and 1, (*b*) 490 and 2.5, (*c*) 490 and 3.33, and (*d*) 560 and 8. Plots are shown at different scales. A single-roll structure occurs at the steady state in each Ar.

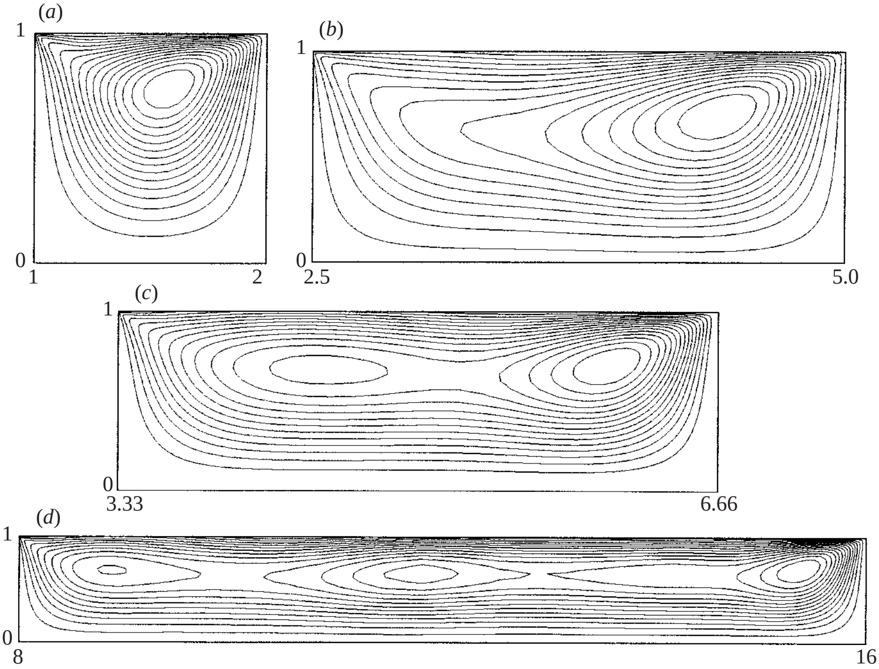

FIGURE 18. Snapshots of meridional streamlines at $\theta = 0$ with $Bi = 0$, various supercritical Re and Ar: (*a*) 800 and 1, (*b*) 525 and 2.5, (*c*) 550 and 3.33, and (*d*) 625 and 8. Multi-cells occur near transition in shallow liquid layers with $Ar \geqslant 3.33$.

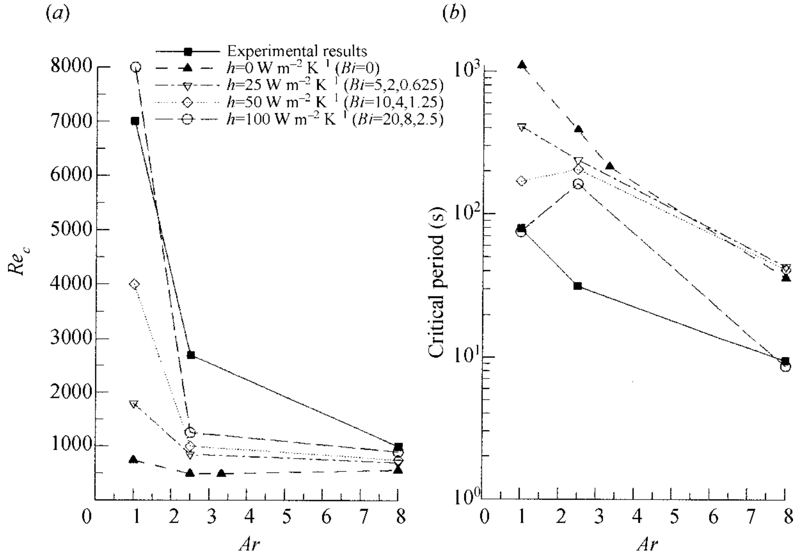

FIGURE 19. Re_c and τ_c corresponding to various Ar at various Bi cooling the free surface. Heat loss from the free surface stabilizes the flow, and Re_c increases with increasing Bi at fixed Ar; τ_c decreases with Ar (Bi) at fixed Bi (Ar). Note that the curves here are for constant h so that Bi decreases along these curves with increasing Ar.

rectangular cavities have in common travelling multi-cells from the cold to hot corners with a standing, pulsating pattern in the third direction.

4.3. *Critical Reynolds numbers and periods*

Figure 19 shows the effect of Bi on Re_c and the critical dimensional period, τ_c. The numerical results with $Bi=0$ are in good qualitative but not in good quantitative agreement with the experiments (see Part 1). The value of h is 25 to 250 W m^{-2} K^{-1} for gases in forced convection. Because of evaporation, the value will be increased substantially. It can be seen that heat loss from the free surface stabilizes the flow, and Re_c increases with increasing Bi, whereas τ_c decreases with increasing Bi. It is observed that better comparison with experiments is achieved at the larger values of Bi.

In Part 1, we argue that the free surface in the experiments is effectively heated by the surroundings. This is modelled here by assuming

$$T_\infty = \frac{(T_\infty^* - T_{cold})}{\Delta T} = \frac{\gamma H}{\nu \mu} \frac{(T_\infty^* - T_{cold})}{Re}.$$

Thus, the last boundary condition in equation (2.6) at $z=1$, with the material parameters listed in table 1 of Part 1, is replaced by

$$\frac{\partial T}{\partial z} = -Bi\left(T - \frac{23600}{Re\,Ar}\right). \tag{4.1}$$

This is the extreme case where T_∞^* is 6 °C higher than T_{cold}. Figure 20 shows the variation of Re_c and τ_c with Bi and $Ar=1$. Re_c and τ_c are very sensitive to Bi due to the constant high temperature of the surroundings, and they approach the experimental results with increasing Bi.

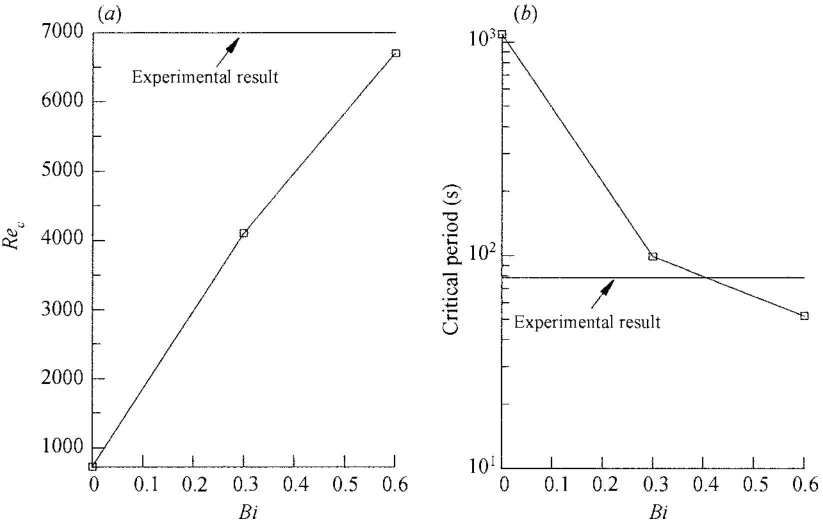

FIGURE 20. Re_c and τ_c with various Bi and $Ar = 1$ in the case of heating from the surroundings to the free surface. The heating stabilizes the flow, and Re_c increases with increasing Bi.

5. Conclusions

Oscillatory thermocapillary convection in open cylindrical containers has been investigated numerically to document its stability characteristics. Frequency F increases with increasing Re near the critical region, while that of supercritical convection approaches a constant value at larger Re.

Five, nine and twelve azimuthal waves near the critical region are found rotating clockwise on the free surface with, respectively, $Ar = 1$, 2.5 and 3.33, while twenty azimuthal nearly standing waves are observed on the free surface with $Ar = 8$. While only a single-roll structure is observed up to Re_c with each Ar, the multi-roll structure appears beyond Re_c in shallow liquid layers with $Ar = 3.33$ and 8. In general, the number of azimuthal waves and multicells increases with increasing Ar, and τ_c decreases with increasing Ar.

Both heat loss from the free surface and heating from the surroundings to the free surface stabilize the flow, and their inclusion is necessary to achieve better quantitative agreement with the experiments. Re_c increases with increasing Bi while τ_c shows the opposite trend.

We gratefully acknowledge computer resources from the Rutgers Computational Grid composed of a Distributed Linux PC Cluster on which all computations were performed.

REFERENCES

CHANG, C. E. & WILCOX, W. R. 1976 Analysis of surface tension driven flow in floating zone melting. *Intl J. Heat Mass Transfer* **19**, 355–366.

CHEN, J. & HWU, F. 1993 Oscillatory thermocapillary flow in a rectangular cavity. *Intl J. Heat Mass Transfer* **36**, 3743–3749.

GARNIER, N. & CHIFFAUDEL, A. 2001 Two dimensional hydrothermal waves in an extended cylindrical vessel. *Eur. Phys. J.* **B19**, 87–95.

KAMOTANI, Y., OSTRACH, S. & MASUD, J. 2000 Microgravity experiments on oscillatory thermocapillary flow in cylindrical containers. *J. Fluid Mech.* **410**, 211–233.

Kamotani, Y., Ostrach, S. & Pline, A. 1995 A thermocapillary convection experiments in microgravity. *J. Heat Transfer* **117**, 611–618.

Kuhlmann, H. & Rath, H. 1993 Hydrodynamic instabilities in cylindrical thermocapillary liquid bridges. *J. Fluid Mech.* **247**, 247–274.

Neitzel, G., Chang, K.-T., Jankowski, D. & Mittelmann, H. 1993 Linear stability theory of thermocapillary convection in a model of the float-zone crystal growth process. *Phys. Fluids* **5**, 108–114.

Patankar, S. 1980 *Numerical Heat Transfer and Fluid Flow*. Mcgraw-Hill.

Peltier, L. & Biringen, S. 1993 Time-dependent thermocapillary convection in a rectangular cavity: Numerical results for a moderate Prandtl number fluid. *J. Fluid Mech.* **257**, 339–357.

Sab, V., Kuhlmann, H. & Rath, H. 1996 Investigation of three-dimensional thermocapillary convection in a cubic container by a multi-grid method. *Intl J. Heat Mass Transfer* **39**, 603–613.

Savino, R. & Monti, R. 1996 Oscillatory Marangoni convection in cylindrical liquid bridges. *Phys. Fluids* **8**, 2906–2922.

Schwabe, D., Zebib, A. & Sim, B.-C. 2003 Oscillatory thermocapillary convection in open cylindrical annuli. Part 1. Experiments under microgravity. *J. Fluid Mech.* **491**, 239–258.

Sim, B.-C. & Zebib, A. 2002*a* Effect of free surface heat loss and rotation on transition to oscillatory thermocapillary convection. *Phys. Fluids* **14**, 225–231.

Sim, B.-C. & Zebib, A. 2002*b* Thermocapillary convection with undeformable curved surfaces in open cylinders. *Intl J. Heat Mass Transfer* **45**, 4983–4994.

Smith, M. & Davis, S. 1983 Instabilities of dynamic thermocapillary liquid layers. Part 1. Convective instabilities. *J. Fluid Mech.* **132**, 119–144.

Wanschura, M., Shevtsova, V., Kuhlmann, H. & Rath, H. 1995 Convective instability mechanisms in thermocapillary liquid bridges. *Phys. Fluids* **7**, 912–925.

Xu, J. & Zebib, A. 1998 Oscillatory two- and three-dimensional thermocapillary convection. *J. Fluid Mech.* **364**, 187–209.